Nanostructures to Engineer 3D Neural-Interfaces: Directing Axonal Navigation toward Successful Bridging of Spinal Segments

Article type: Full Paper *Special Issue- Advanced Functional Materials Solutions to Engineering the Neural Interface*

WILEY-VCH

Nanostructures to Engineer 3D Neural-Interfaces: Directing Axonal Navigation towards Successful Bridging of Spinal Segments

Emily R. Aurand[1], Sadaf Usmani[1], Manuela Medelin, Denis Scaini, Susanna Bosi, Federica B. Rosselli, Sandro Donato, Giuliana Tromba, Maurizio Prato, Laura Ballerini**

Dr. E. R. Aurand, S. Usmani, Dr. F. B. Rosselli, Prof. L. Ballerini

Scuola Internazionale Superiore di Studi Avanzati (SISSA) Via Bonomea, 265 - 34136 Trieste ITALY

Dr. M. Medelin, Dr. D. Scaini, Dr. S. Bosi, Prof. M. Prato

University of Trieste, Via Giorgieri, 1 – 34127 Trieste ITALY

Prof. M. Prato

Carbon Nanobiotechnology Laboratory, CIC biomaGUNE, Paseo de Miramón 182 20009 Donostia-San Sebastián (Spain)

Basque Fdn Sci, Ikerbasque, Bilbao 48013 (Spain)

Dr. S. Donato, Dr. G. Tromba

Elettra-Sincrotrone Trieste S.C.p.A. Strada Statale 14 - km 163,5 in AREA Science Park 34149 Basovizza, Trieste ITALY

[1] These authors contributed equally to the work

*Corresponding authors Laura Ballerini SISSA via Bonomea 265 341236 Trieste Italy +30 040 3787779 laura.ballerini@sissa.it ; prato@units.it

Keywords: carbon nanotubes, spinal cord, organotypic cultures, electrophysiology, elastomeric scaffolds three-dimensional X-ray micro-tomography

Neural interfaces are the core of prosthetic devices, such as implantable stimulating electrodes or brain-machine interfaces, and are increasingly designed for assisting rehabilitation and for promoting neural plasticity. Thus, beyond the classical neuro-prosthetic concept of stimulating and/or recording devices, modern technology is pursuing toward ideal bio/electrode interfaces with improved adaptability to the brain tissue. Advances in material research are crucial in these efforts and new developments are drawing from engineering and neural interface technologies. We exploit here a micro-porous, self-standing, three-dimensional (3D) interface made of polydimethylsiloxane (PDMS) and implemented at the interfacing surfaces with novel conductive nano-topographies (carbon nanotubes). We characterize the scaffolds porosity by 3D X-ray micro-tomography. We use these structures to interface axons regenerated from cultured spinal explants and we show that engineering PDMS 3D interfaces with carbon nanotubes effectively changes the efficacy of regenerating fibers to target and re-connect segregated explant pairs. We show, when the spinal tissue is interfaced to PDMS enriched by carbon nanotubes, an improved electrophysiological performance that may favor the use of our substrates as regenerative interfaces. We implant the materials in the rat brain and we report a limited tissue reaction surrounding the implants at 2, 4 and 8 weeks from surgery.

WILEY-VCH

1. Introduction

Neural prostheses are artificial, implantable devices designed to restore functions that are lost in injured or diseased central nervous system (CNS). In manufacturing CNS implants, the tissue-electrode interface represents a crucial component that limits the performance, the longevity and the stability of prostheses.[1,2] More recently, interfaces are increasingly engineered not only to improve neural recording and stimulation, but to promote neural regeneration together with the therapeutic delivery of bioactive molecules. In these developments, the interface architecture is redesigned by the use of tailored materials with nano-scale geometries mimicking topographical cues able to improve neuronal growth, viability, and adhesion.[3-5] In further advances, regenerative interfaces are cellularized by the inclusion of cell grafts to provide a target site for re-innervation. Thus, interfaces of the future may require more sophisticated neural-material hybrids tested in the laboratory to create three-dimensional constructs that are more easily recognized by brain networks.[4,6]

We recently developed a micro-porous, self–standing, elastomeric scaffold made by polydimethylsiloxane (PDMS) with micrometric cavities generated upon dissolving a sugar template that was previously embedded in PDMS and we further nanostructured the scaffold by means of carbon nanotubes, implementing the polymer with novel nano-topographies with which cells can actively interact.[7]

Carbon nanotubes have repeatedly been shown to provide an electrically favorable environment to potentiate neuronal signaling.[8-13] Improved signaling between neural cells can potentially aid in cell maturation and in the formation of complex, functional neuronal networks.[10,11] A polymer material incorporated with

carbon nanotubes is, therefore, likely much more advantageous when attempting to build an interactive interface to improve axonal growth and guide synapse formation and function.

Organotypic spinal slice cultures represent a complex *in vitro* model where both sensory-motor cytoarchitecture and electrical properties are retained in a 3D-fashion.[10,14,15] We recently used such a model to test the ability of pure carbon nano-fiber 3D interfaces in promoting successful reconnection of separated spinal explants *in vitro*.[16] Here, we exploit cultured slices used as pairs to test 3D PDMS interfaces with or without carbon nanotubes. Previous studies have shown that spinal slices separated at distances more than 300 µm fail to reconnect under basal conditions,[7,15-18] despite the huge outgrowth of nerve fibers,[10,14,16] allowing for the investigation of potential reconnection in the presence of efficacious cues. In this study, we investigate by electrophysiology, immunofluorescence and confocal microscopy, organotypic slices interfaced to 3D scaffolds made of polymer-alone or polymer and nanotubes. In particular, we address the navigation within the artificial structures of neuronal fibers exiting the slices and we correlate neurite distribution at the interface with functional slice-to-slice reconnection.

We also investigate the biocompatibility of the PDMS constructs *in vivo* upon implantation into adult rat visual cortex[16] observed at 2^{nd}, 4^{th}, and 8^{th} week post-surgery time-points. We use immunofluorescence labeling to quantify the density of inflammatory response-mediating cells surrounding the implant material and of neuronal markers to assess the level of cellular infiltration into the scaffold *in situ*.

Our data indicate that the incorporation of carbon nanotubes into a three-dimensional polymer construct confers increased neuronal activity in the spinal

networks developed at the interface and guides re-growing axons towards functional reconnection of separated spinal explants. We also suggest that PDMS with carbon nanotube materials elicit minimal immune response following implantation into the CNS.

2. Results and Discussion

Scaffolds used to interface organotypic slice cultures: a micro-tomography analysis

Two different, micro-porous, free-standing, elastomeric scaffolds, able to sustain the development of organotypic slices, were developed following the procedure described in our previous work.[7] PDMS scaffolds are the negative replica of a generating sugar framework; this allows for fabrication of 3D sponge-like structures characterized by irregular porosity, with random channels connecting the pores. Within the same fabrication procedure, we generate micrometric cavities by a sugar mold previously mixed to multi walled carbon nanotubes[7] (MWCNTs, **Figure 1**). This permits the formation of 3D sponges with the pore surfaces layered by a MWCNT carpet, stably trapped in the PDMS matrix.[7] Scanning electron microscopy analysis of the PDMS scaffolds and of the PDMS decorated by the MWCNTs (PDMS+CNT) reveals similar “sponge-like” morphologies (Figure 1a and Figure 1b), with the PDMS+CNT showing the presence of a layer of MWCNTs lining the inner facets of the pores (Figure 1b**,** inset).

Three-dimensional X-ray micro-tomography (µCT) reconstructions allow a comparison of the inner pore and channel morphologies of the two materials (Figure 1c). These measures show that both scaffolds display similar hollow features. Regarding the general porosity, PDMS scaffolds (n=3) contain 50±11% empty volume and similarly, in PDMS+CNT scaffolds (n=3), the empty volume is 54±6%

(Figure 1d). Interestingly, the isotropic index is 0.89±0.03 and 0.91±0.02 for PDMS and PDMS+CNT samples, respectively. This reveals that pore shape and channel directions are both isotropic traits of the manufactured scaffolds (Figure 1d). The diameter of the inscribed sphere (mean ±SD) in PDMS samples is 29±8 µm, with the interconnecting channel mean size of 16±1 µm, while in PDMS+CNT scaffolds the mean inscribed sphere diameter is 23±2 µm, with 14±1 µm channel size (Figure 1e). These values were not significantly different (P=0.25 and P=0.14 for pores and throats, respectively; Figure 1e).

After this characterization, PDMS and PDMS+CNT substrates were used over extended periods to interface the development of neural networks in long-term, co-cultured pairs of mouse organotypic spinal cord explants.[10,16]

Spinal explants interfaced to the PDMS and PDMS+CNT constructs: axonal colonization of the interfaces in the third dimension

Spinal organotypic slices after >10 days of *in vitro* development exhibit a characteristic outgrowth of nerve fibers[10,16] and a rich neurite network observed in PDMS and PDMS+CNT conditions (**Figure 2a and b**). Pairs of slices, when interfaced to PDMS or to PDMS+CNT, sprout neuronal processes that rapidly invade the 3D structure of the interfaces. In this set of experiments, we explore the infiltration of fibers within the sponges [10,16] and we investigate their patterns of growth by confocal microscopy and comparing the regions of interest (ROI: 640×640 µm; 20 and 28 ROI, n=5 and n=9 cultures, PDMS and PDMS+CNT respectively) sampled from the area surrounding the slice explants.[16]

To determine if there were any differences between the PDMS and PDMS+CNT substrates' ability to guide neuronal process distribution, we acquired z-stacks to reconstruct the sampled ROIs (Figure 2a and Figure 2b, right panels) and measured the thickness through which the β-tubulin III-positive neurites were detectable within the interface materials.

Image stacks demonstrate that neurites are distributed in complex network formations across the surface of the substrates, reaching varying depths into the manufactured interfaces (Figure 2a and Figure 2b, right panels). Interestingly, we found that the depth through which neurites are travelling in the PDMS substrates (see Figure 2a and Figure 2b**,** bottom insets to right panels) is significantly greater than the neurite distribution in PDMS+CNT substrates (105.5±8.6 μm and 52.7±3.9 μm, respectively, $P<0.001$; Figure 2c), despite the absence of any significant difference in substrate pore/channel size (Figure 1e), excluding that a mere variability (in the micron scale) of the PDMS- and PDMS+CNT-interfaced skeleton influenced the permeation of growing neurites.

To further explore the differences in fiber outgrowth and morphology within the 3D interfaces, we also quantified the overall neurite density and the degree of dispersion.[16] In fact, depending on the substrate that supports the elongation of neuronal projections exiting the interfaced spinal explant, neural fibers can be organized in thick bundles of aligned processes[10] or in complex webs of randomly oriented fibers.[16]

First, we estimated neuronal fiber density.[16] By this procedure, we detect no differences in the amount of β-tubulin III-positive area between PDMS (28.05±2.89% positive area, n=29 ROIs acquired from n=10 cultures) and PDMS+CNT

(26.77±3.53% positive area, n=20 ROIs acquired from n=6 cultures) samples, suggesting that the amount of β-tubulin III-positive fibers outgrowing from the slices is similar (Figure 2d), although differently scattered in the third dimension (Figure 2c).

In a recent work,[16] we showed that pure carbon nanotube 3D scaffolds, when interfaced to cultured spinal slices, shape the neuronal processes extending from organotypic slices into a mesh-like structure, compared to bundled fasciculations that occur when slices are cultured interfaced to fibrin glue layered on 2D glass coverslips.[16] We perform a similar analysis here to further investigate if this reduction in fiber orientation is tied more closely to the porous nature of the substrate or directly to the presence of carbon nanotubes. When fiber directionality is assessed in terms of degree of angular dispersion,[16] we find no differences in the mean dispersion angle values of the two samples (average degree of dispersion: 17°±2° for PDMS, n=28 ROIs; 16°±3° for PDMS+CNT, n=20 ROIs; Figure 2e). The relatively high degree of dispersion (>15°) in both samples confirms our previous experiments[16] by indicating that, once interfaced to 3D structures, the majority of fibers are not oriented in “bundle-like” assemblies but, instead, they tend to form a random network.[16]

To summarize, both constructs support and attract neuronal process growth, as shown by the comparable β-tubulin III-positive area measured, but the presence of MWCNTs on the porous surface seems to limit, maybe by adhesion processes, the growth of neural fibers deep within the third dimension of the structure. Both porous constructs also favor the formation of intricate networks of variably oriented fibers, regardless the presence of MWCNTs, characterized by fewer thick, aligned bundles when compared to traditional 2D interfaces.[10,16]

Engineering PDMS interfaces by carbon nanotubes affects the functional re-wiring of segregated spinal explants

After characterizing the scaffolds' structure and the morphology of the neurite network infiltrating the structures upon interfacing spinal slices for >1 week, our primary interest is to investigate the *in vitro* effects of PDMS and PDMS+CNT interfaces on spinal network activity and their ability to promote functional re-connections between slice pairs.

Cultured spinal explants display prominent spontaneous electrical activity and well characterized motor (ventral) outputs.[14,16] We monitored extracellular potentials (local field potentials, LFPs) by placing electrodes in the ventral regions of each slice (within 20-100 µm of the ventral fissure; sketched in **Figure 3a**).

To examine the functional impact of interfacing slices with the two different materials we use the glycine/$GABA_A$ receptor antagonists strychnine (1 µM) and bicuculline (20 µM) to weaken synaptic inhibition in PDMS and PDMS+CNT slice pairs (n=13 and n=16 cultures, respectively). These antagonists of inhibitory synapses are known to shift electrical motor outputs from random bursting to synchrony, as previously reported for the entire spinal cord[19] and for organotypic spinal slices,[20, 21] leading, in all cultures tested, to the emergence of a slow-pace bursting (see sample tracings in Figure 3b).

A characterizing feature of spinal disinhibited rhythm is the frequency of bursting episodes that we quantified by measuring the inter-event intervals (IEI). A direct comparison of IEI measured in the PDMS or PDMS+CNT constructs, reveals that the frequency distribution of IEI values is significantly shifted to the left in spinal

slices cultured in the presence of carbon nanotubes (P<0.001; Figure 3c), the average IEI values being 7.0±0.6 s in PDMS+CNT (n=28 slices) and 11.2±1.1 s in PDMS (n=23 slices). Such an increase in rhythmic burst activity is reminiscent of the improved excitability usually detected when interfacing spinal slices to MWCNT carpets.[10] We can speculate that the MWCNTs exposed on the PDMS surfaces alter synaptic connectivity and/or firing activity in cultured slices,[10] possibly at the layer of neurons in direct contact to MWCNTs, affecting the excitability of the spinal networks.[10] However, we cannot exclude that the increased bursting activity is also reflecting an improved functional coupling among pairs of slices in the presence of carbon nanotubes. That is, when interfaced to PDMS+CNT, neuronal processes have more probability to interweave within the construct and to synapse to the co-cultured spinal tissue, compared to those interfaced to PDMS alone. To clarify this issue, we further studied the functional connectivity between the two slices assessing, by cross-correlation analysis of the disinhibited bursting, the presence of synchronous ventral outputs.[15,16]

Ventral LFP recordings of disinhibited bursts were taken simultaneously from co-cultured slices in PDMS or in PDMS+CNT (see Figure 3a for the experimental set-up and **Figure 4a** for an example of the recordings). We use a MATLAB algorithm[16] to calculate the Pearson cross-correlation coefficient (CCF) between the two co-cultured slices and to determine whether the CCF values obtained are significantly larger than that expected by chance, thus supporting the presence of functional contacts between the explants. An example of this analysis, performed for the recordings shown in Figure 4a, is shown by the plots of Figure 4b**,** where the distribution of CCFs obtained by randomly sampling the two time series in each

experiment [16] is compared to the average CCF computed sampling consecutive time windows (the red line in the plots of Figure 4b). In PDMS+CNT, 81% of the co-cultured explants are correlated, displaying CCF values significantly larger than that expected by chance; on the contrary, in PDMS, correlated slices are detected only in 37.5% of samples (a significant difference; $P<0.05$, Figure 4c). These results suggest that there are increased functional connections between the spinal slices interfaced with CNT-containing substrates, compared with those interfaced by PDMS alone. The low probability of re-connection in the PDMS interfaces is not surprising and is in line with our preliminary findings:[16] slices cultured side-by-side in pairs at distances known to inhibit functional reconnection in basal conditions[15,16] reconnect with a low probability even in the presence of 3D PDMS interfaces.[16] In our experiments, the average measured distance between slices is 1.9±0.1 mm for PDMS (n=7) and 1.6±0.1 mm for PDMS+CNT (n=15). The emergence of functional coupling is unrelated to the inter-slice distance (Figure 4d; note that filled symbols indicate functional correlated pairs measured as described above and in Figure 4b; $r_{PDMS+CNT}$=0.30±0.30, n=15; r_{PDMS}=0.22±0-29, n=7), as well as to the age in culture (sampled from 10 to 23 days; Figure 4e $r_{PDMS+CNT}$=0.20±0.29, n=16; r_{PDMS}=–0.08±0.29, n=8).

Engineering PDMS 3D interfaces with MWCNTs effectively changes the efficacy of regenerating fibers to target and re-connect segregated explants. We also show an improved electrophysiological performance that may favor the use of our substrates as regenerative interfaces.

In our previous study we reported that when interfacing pairs of spinal explants to scaffolds, the improved directionality dispersion and the third dimensional

outgrowth of neurites are needed to improve the fraction of re-connected pairs, regardless the amount of β-tubulin III-positive area.[16] However, 3D constructs, such as the PDMS interface used here, were not able to replicate the ability of pure 3D MWCNTs sponges[16] in reconnecting separated spinal slices by dispersed webs of axons, leaving unresolved what properties of the latter were making the difference: the tubular morphology and elastic properties of frestanding MWCNTs skeleton[16] or the physical and chemical properties of the MWCNT material in the third dimension?[12,16] Here we compare, for the first time, two PDMS-based interfaces exibiting highly similar scaffold structures but for the presence of a layer of MWCNTs. We used PDMS elastomer since this material is a standard in microfabrication or microfluidics developments in biological applications, due to the PDMS simple manufacturing together with its gas permeability, optical transparency, flexibility.[22,23,24] In addition, this elastomer has been recently engineered in 2D devices showing excellent mechanical flexibility and leading to soft implants integrated in the subdural space.[25] PDMS has also been filled with MWCNTs using microntact printing and casting mold techniques[26] to provide conductive PDMS patterns, with potential applications in biology. Here, by entrapment in the PDMS surface of nano-features such as carbon nanotubes, we have engineered an interfacing grid with the ability to direct the formation of reconnecting webs of neurites. The interactions among the geometry, chemistry and the numerous physical and biological factors translating the exposure to MWCNTs into axonal regrowth and synapse formation are unknown. Interestingly, we found that neurites penetrated significantly greater depths into PDMS substrates compared with the PDMS+CNT substrates. We speculate that the presence of MWCNTs improve neurites

mechanical tight associations with the interface, whereas in the case of PDMS, neurites tend to drop down into the pores following gravity, without associating with the material. That the neurite-MWCNT association is the rationale for the neuronal processes remaining within the first layers of the scaffold is supported by previous works which show that MWCNTs form extremely tight contacts with biological membranes.[8,10] We exclude large differences in the scaffolds' mechanical features, since in both PDMS and PDMS+CNT elasticity is due to the porosity of the structure.[7] In our previous study, we reported for similar porous scaffolds a Young's modulus within the range of that estimated in rodent and human brains. [7] Our *in vitro* results show that both scaffolds are of a mechanical stiffness conducive to neural tissue growth and sustainment.

We suggest the use of 3D PDMS scaffolds incorporated with MWCNTs as a potential candidate for manufacturing regenerating interfaces. The increasing application of nanomaterial-related technologies for engineering brain interfaces may thus ameliorate some intrinsic features of interfacing devices (such as the stability or the charge transfer to and from neurons),[27] as well as their ability to facilitate recovery of function via guiding regenerating fibers.

Biocompatibility of PDMS+CNT implanted in vivo

Towards further biomedical applications, any new device needs to be challenged with the biological milieu *in vivo*. Given the beneficial interactions *in vitro* of PDMS+CNT materials compared with PDMS-alone, in the last set of experiments we assess the tissue response to PDMS+CNT implantation in the cortex of adult rats.

The use of PDMS as inert polymer for generating implantable scaffolds is traditionally accepted[28] nonetheless advantages and limitations of any suitable material need to be evaluated when micro-fabrication technologies are designed for biological applications.[29]

Unfortunately, in our early observations, we detected a complete absence of interaction of the brain tissue with implanted PDMS scaffolds when not incorporating MWCNTs (n=2 animals; data not shown). In these animals, after 2 and 8 weeks (18 sections) post-surgery, the lack of integration of the PDMS scaffold with the surrounding cortical tissue is to an extent that the material no longer remains within the tissue following sectioning and subsequent histological processing for immunofluorescence labeling. This makes it virtually impossible to quantify the response in the surrounding tissue at the immediate interface with the material; i.e., we cannot predict, for example, how much of the glial scar, is removed along with the implanted material during the tissue processing. These results were not entirely unexpected, as other studies have demonstrated a lack of PDMS integration with surrounding tissues when the PDMS material is not modified (such as via etching or the incorporation of adhesion molecules).[30,31] Because the *in vitro* results suggest that MWCNTs have a significant functional benefit over PDMS-alone substrates, we thus focused our biocompatibility study on the PDMS+CNT material.

We measured the surrounding microenvironment responses to PDMS+CNT implants, in particular we focus on the distribution patterns and infiltration of microglia together with astrocyte aggregation at the interface.[16,32-34]

Electrodes are common neural-implanted devices; extensive reporting in the literature illustrates that many, if not most, implanted electrodes have reduced

functionality over time due to the tissue response and glial scarring, an indicator of inadequate biocompatibility.[35-38] Glial scar formation typically occurs during the first two to four weeks following material insertion and is characterized by a dense reactive astrocyte and microglia region that can extend beyond 100 µm from the implant.[35,36,38-40] This region can also undergo to relative neurodegeneration with a decrease in the number of local neurons.[35,36]

We implanted PDMS+CNT scaffolds into the adult rat visual cortex.[16] Rats were sacrificed at 2 weeks (n=3), 4 weeks (n=3), and 8 weeks (n=3) post-implantation. Brain tissue sections were immunolabeled for astrocytes and microglia (**Figure 5a** and 5b) using antibodies against GFAP and Iba1, respectively, to determine the level of tissue reactivity surrounding the implanted material and any presence of a glial scar. Tissue sections were also immunolabeled with β-tubulin III and NeuN, to determine if any neurons were able to infiltrate the material.[16] Overall, the immunoreactivity of astrocytes and microglia surrounding the implanted material suggests a generally low immune response. In fact, as shown in Figure 5a, the increased GFAP immunoreactivity surrounding the implant is substantially limited to the first 50 to 60 µm from the implant edge at all time points (quantifyed in Figure 5c). Further analysis reveals that, while the mean intensity up to 50 µm from the implant is not different between the three time points investigated ($P=0.119$), the mean intensity up to 150 µm, (namely, to larger distances from the implant edge), of the GFAP fluorescence is significantly ($P\leq0.001$) lower in 4 and 8 weeks animals when compared to 2 weeks (2 weeks = 1.73±0.02 a.u., 4 weeks = 1.55±0.02 a.u., 8 weeks = 1.57±0.03 a.u.; Figure 5c). This suggests that, generally, the glial response in the surrounding tissue is likely decreasing when moving past the acute, inflammatory

phase of the tissue reactivity. Regarding microglia cells, Iba1 immunoreactivity surrounding the implant (up to 500 μm) significantly decreases over time (Figure 5b and d). When measured, the average intensity is 0.22±0.02 a.u. at 2 weeks, 0.14±0.02 a.u. at 4 weeks; P=0.004 and 0.08±0.01 a.u. at 8 weeks (P≤0.001 vs. 2 weeks and P=0.02 vs. 4 weeks). Iba1-positive microglia are observed to have infiltrated the implant material as early as 2 weeks post-implantation and continue to reside within the material at 8 weeks post-implantation.

Compared with other reports regarding the tissue response to cortical implants, we observe a general decrease in GFAP-positive astrocyte labeling from 2 to 8 weeks after implantation and, by 8 weeks post-implantation, limited to the area immediately surrounding the implanted material (Figure 5a).[36,37,40,41] In accordance with a reduction in inflammatory phase, there is a significant decrease in the intensity of Iba1-positive microglia labeling surrounding the implant over time. This is in contrast to the persistent upregulation of microglia associated with compromised biocompatibility and foreign body rejection often seen with implanted electrodes.[35-37,40-42] Interestingly, we observe Iba1 immunoreactivity inside the implanted material at all time-points (Figure 5b). It is interesting to note that an increased Iba1 immunoreactivity within MWCNTs, both when used as substrates[11] and as 3D scaffolds[16] has been observed before, without any indications that this increase is associated with an immune response. *In vitro,*[11] we observed an increase in Iba1-positive cell density in dissociated neural cells with an insubstantial immune response, while *in vivo*[16] the colonization of the material with native cells, as described here with the PDMS+CNT material, may sustain biocompatibility with neural tissue.

Further research will be necessary to establish a thorough response profile and the true functionality of this material *in vivo*.

Additionally, in order to define whether the PDMS+CNT scaffold was fully integrated within the neural tissue, we investigated the presence of neurons within the material.[16] We observe β-tubulin III-positive neuronal processes (**Figure 6a**) permeating the 3D scaffold at the three time points studied (27%: 6 of 22 horizontal slices, 57%: 16 of 28 horizontal slices and 44%: 8 of 18 horizontal slices at 2, 4 and 8 weeks post-implantation, respectively; Figure 6c). Therefore, β-tubulin III-positive cells invade the implanted material as early as 2 weeks post-implantation and their presence increases at later stages, though without reaching a statistical difference. In a subset of slices (2 animals, 2 weeks, n=8), we provide further evidence of infiltrated neuronal cells by exploiting the specific neuronal nuclear marker, NeuN.[16] In these experiments, we detect NeuN-positive neurons within the construct, as shown in an exemplifying image in Figure 6b. The presence of neuronal cells, perhaps migrating neuroblasts, within the implant is surprising, however is in agreement with our recent report describing NeuN-positive cells localized in implanted MWCNT based scaffolds[16]. These findings, together with our previous work demonstrating very similar GFAP and Iba1 immunoreactivity in MWCNT-alone scaffolds,[16] confirm the MWCNTs-based materials as biocompatible 3D scaffolds and support their application as neural interfaces.

3. Conclusion

Controlled engineering of polymeric interfaces into 3D porous constructs favors the formation of intricate networks of variably oriented axons re-growing from the interfaced spinal tissues. The further incorporation of MWCNTs promotes the

manufacturing of more efficient regenerating interfaces and guiding of regenerating axons to targets. Generally, the possibility to decorate elastomeric structures with nanomaterials implements the adhesion of axons to the interfacing devices and can be used to fabricate conductive pathways within a 3D construct. In this work, a novel 3D structure was interfaced to spinal explants *in vitro* and its biocompatibility was assessed *in vivo*. The presented results hold the potential to exploit the use of 3D hybrids and carbon nanotubes in the area of (nano)engineering regenerative interfaces.

4. Experimental Section

PDMS 3D interface fabrication

Three-dimensional PDMS scaffolds are free-standing, porous structures made by polydimethylsiloxane (PDMS; Sylgard® 184, Down Corning Co.), an elastomeric material commonly used in biomedical applications.[22-24,43] The fabrication procedures involve water dissolution of a sugar scaffold, resulting in a cast PDMS framework consisting of interconnected cavities as previous described.[7] In brief, 500 mg of food-approved sugar was passed through a №. 60 mesh sieve (Sigma-Aldrich) and mixed with 20 µL of deionized water, placed in a silicon mold, and subsequently dried at 65 °C for 30 minutes. PDMS was vacuum-forced to percolate inside the resulting sugar framework until all spaces were filled, and cured in an oven at 85 °C for 1 hour. After cooling, the sugar was dissolved by submersing the sample in distilled water overnight. The water-driven dissolution of sugar grains produces a network of interconnected micro-pores inside the PDMS scaffold.

MWCNTs, 20-–30 nm in diameter (Nanostructured & Amorphous Materials, Inc.), were prepared as previously reported,[9] briefly MWCNTs were functionalized

using 1,3-dipolar cycloaddition with heptanal and sarcosine at 180 °C for 24 h in o-dichlorobenzene (ODCB) as solvent. MWCNTs were incorporated in PDMS scaffolds by mixing functionalized MWCNTs (15 mg) with the sugar (500 mg, sifted as described above). Before use, scaffolds were sonicated in distilled water for 20 minutes, dehydrated in ethanol solution (99.5%), and dried in an oven at 65 °C for 2 hours. Scaffold layers of about 5 mm × 5 mm in lateral dimensions and 300 µm in thickness were extracted from the bulky material using a vibratome (Leica VT 1000S, Leica Biosystems) and mounted on thin glass coverslips (24×12×0.2 mm^3) using PDMS (Sylgard® 184, Down Corning Co.).

Prior to use, PDMS and PDMS+CNT substrates were treated with low-pressure air plasma for 5 minutes at high power using a PDC-32G Plasma Cleaner (Harrick Plasma) and sterilized under UV light for 20 minutes. PDMS is characterized by pronounced hydrophobicity – the major drawback for use of the material for *in vitro* and *in vivo* applications – which was addressed by an oxygen plasma treatment. This treatment turns the PDMS surface hydrophilic by introducing hydroxyl groups *en masse* to the surface.[22]

Synchrotron Radiation (SR) computed micro-tomography and Scanning electron microscopy (SEM)

To characterize 3D PDMS and PDMS+CNT scaffolds, we performed computed micro-tomography (µCT) studies. X-ray µCT experiments were carried out at the SYRMEP beamline of the ELETTRA synchrotron light source (Trieste, Italy). In order to enhance the image contrast, a single distance phase retrieval pre-processing algorithm[44] was applied to the CT projections, prior to the reconstruction procedure

based on the standard Filtered Back Projection approach. The experiment was done in the white beam configuration mode with a polychromatic spectrum. We applied filters for low energies (1 mm of aluminum) resulting in a hardened beam with average beam energy of 22 keV. The detecting system consisted in a sCMOS chip based camera, placed at 10 cm away from the sample, and coupled with a high numerical aperture optic so the resulting pixel size was set to 0.9 µm. Each dataset consists in 1800 projections covering a total angle range of 180° with an acquisition time of 0.25 seconds per projection. The application of the tomographic method provides the benefit of reconstructing, in a non-destructive manner, the complex 3D organization of pores and channels inside the material and to provide a map of the void spaces. Three dimensional volumes were obtained reconstructing the series of 2D projections using the STP (SYRMEP Tomo Project) software[45] and then analysis was performed with Pore3D software library.[46] The porous matrix was evaluated in terms of number and dimension of pores and throats, connectivity density and anisotropy index.[47] Pore and throat numbers and size distributions were obtained following a skeleton analysis[48] and using the concept of maximal inscribed sphere, while connectivity density, a simple global measure of connectivity which gives higher values for better-connected structures and lower values for poorly connected structures, was evaluated finding the Euler characteristic.[47]

PDMS and PDMS+CNT scaffolds morphologies were assessed via scanning electron microscopy (SEM). Images were acquired collecting secondary electrons on a Gemini SUPRA 40 SEM (Carl Zeiss NTS GmbH, Oberkochen, Germany). Bare scaffolds were mounted on conductive double side carbon tape (Ted Pella, Inc.,

USA) and imaged at 5 keV. Prior to SEM characterization samples were metalized with a thin layer of gold (<10 nm) using a metal sputter coater (Polaron SC7620).

Organotypic spinal cord slice preparation and culture

Organotypic slice cultures were obtained as previously described.[10] Briefly, embryos at embryonic day 12 (E12), were isolated from timed-pregnant mice (C57Bl) euthanized by CO_2 overdose and decapitation. Spinal columns were isolated and the low thoracic to high lumbar regions were dissected away from the surrounding tissue. By tissue-chopper we sliced this tissue transversely (275 µm) and further isolated the spinal cord and dorsal root ganglia tissue. Spinal cord slices were placed in cold GBSS and refrigerated for 1 hour prior to placement on the substrates. Pairs of spinal cord slices were embedded into a thick matrix of chicken plasma (Rockland) and thrombin (Sigma) clot and placed upon the PDMS and PDMS+CNT substrates the distance between the slice pairs being within the range of 1.0 to 2.5 mm (inter-slice distance measured from center of the two slices); slice pairs not falling within this distances were discarded. The specified distance was necessary to ensure homogeneity in experimental conditions between the two populations (PDMS and PDMS+CNT) for electrophysiological and immunofluorescence experiments. Slice pairs were cultured for 10 to 22 days *in vitro* (DIV) in plastic Nunc tubes with 1.5 mL medium containing 67% DMEM (Invitrogen), 8% sterile water for tissue culture, 25% fetal bovine serum (Invitrogen), and 25 ng/mL nerve growth factor (Alomone Laboratories); osmolarity, 300 mOsm; pH 7.35. The tubes were kept in a roller drum rotating 120 times per hour at 37 °C in humidified conditions with 5% CO_2.

Electrophysiological recordings and analysis

Organotypic slice cultures at >10 DIV were mounted in a Perspex® recording chamber, installed on an upright microscope (Leica DM LFS) with a continuous superfusion of control physiological saline solution containing (in mM): 152 NaCl, 4 KCl, 1 $MgCl_2$, 2 $CaCl_2$, 10 HEPES, and 10 Glucose; pH adjusted to 7.4 with NaOH. Simultaneous extracellular recordings were obtained at room temperature (RT; 20 to 22 °C) using low resistance glass micropipettes (4 to 6 MΩ) filled with 20 mM KCl saline solution. The electrodes were advanced manually using micromanipulators (Luigs and Neumann SM1, Germany) into the ventral region in both slices. Voltage local field potentials (LFP), as a consequence of synaptic activity and action potential firing, were recorded in regions 20 to 100 µm from the ventral fissure.[23,43] The recorded signals were amplified with the offset neutralized manually through the amplifier by current injection (Axopatch 1D; Axon Instruments). Signal recordings were acquired using the Clampex 8.2 software (pClamp suite, Axon Instruments) and digitized at 10 kHz (Digidata 1322A, Axon Instruments), filtered lowpass at 2 kHz. Strychnine and bicuculline (1 µM and 20 µM, respectively) were administered into the bath to induce disinhibited rhythmic bursting.[49] Disinhibited bursts were evaluated by mean inter-event interval analysis (the time between the onset of each burst; we used ≥20 bursts for each measure).

Disinhibited burst LFPs obtained from each spinal slice were low-pass filtered at 3 Hz and the data reduced and imported to MATLAB.[16] We further assessed the synchrony between the bursting activities of the two explants in each pair by computing the Pearson correlation coefficient between the two voltage time series.

The statistical significance of the correlation coefficient was determined by performing a permutation test,[16] that allowed to measure the distribution of correlation coefficients that one would expect to observe if the voltage signals recorded from a pair of explants happened to correlate purely by chance. By measuring how likely it was for the values of this null distribution to be larger or equal than the real correlation coefficient, it was possible to understand whether the correlation between the pair of time series was significantly larger than expected by chance. This procedure allowed for determining what fraction of co-cultured slices exhibited a significantly synchronous bursting activity, for all the tested conditions. A full amelioration of the cross correlation analysis can be found in Usmani, et al. 2016.[16] The fraction of significantly correlated pairs ($P<0.05$) was compared between PDMS and PDMS+CNT groups by performing a *chi*-squared test for homogeneity.

Spinal culture immunohistochemistry

Following electrophysiological recordings, organotypic spinal slices were fixed at room temperature for 1 h in 4% formaldehyde (prepared from fresh paraformaldehyde, PFA) in PBS (Sigma) then washed with PBS. Samples were treated with 0.1 M glycine in PBS for 5 minutes to quench free aldehyde groups. Samples were incubated for 30 min in protein blocking solution (5% BSA, Sigma-Aldrich, 0.3% Triton X-100, Carlo Erba, 1% Fetal Bovine Serum, Gibco in PBS). Subsequently, samples were incubated with the primary antibodies, rabbit anti-β-tubulin III (polyclonal, Sigma-Aldrich Cat# T2200, RRID: AB_262133; used at 1:200) prepared in PBS with 5% FBS at 4 °C, overnight. After thorough washing in PBS,

samples were incubated in secondary antibodies: goat anti-rabbit AlexaFluor 594 (polyclonal, Thermo Fisher Scientific Cat# R37117, RRID: AB_2556545; used at 1:500) and labeled with 4',6-Diamidino-2-Phenylindole, Dilactate (DAPI; monoclonal, Thermo Fisher Scientific Cat# D3571, RRID: AB_2307445; used at 1:500) prepared in PBS with 5% FBS at room temperature for 2 h. Following secondary antibody incubation, samples were rigorously washed in PBS and briefly with water before mounting on glass coverslips using Vectashield® mounting medium (Vector laboratories).

Spinal culture imaging and analysis

Images of immunolabeled organotypic spinal slice pairs were acquired using a Leica DM6000 epifluorescence microscope using a 2.5× dry objective. This low magnification allowed for visualizing both slices in the same field in order to identify slice location and to measure inter-slice distance. Further, a Nikon C2 confocal microscope was used to acquire higher quality images of the neurites spreading three-dimensionally into the substrate (40× oil objective, N.A. 1.3, oil mounting medium R.I. 1.515). The total stack thickness was set in order to obtain all β-tubulin III-positive processes from the sample with a z-step of 1 µm. Analysis and 3D reconstruction of the image stack was accomplished using NIS-Elements AR software (Nikon), Volocity (PerkinElmer), and the open source image processing package, FIJI (http://fiji.sc/Fiji).

Assessment of any differences in the 3D distribution of neuronal processes on PDMS and PDMS+CNT substrates was evaluated by considering image stacks taken from regions central (area between slices) and peripheral (at the substrate edge) to

the slices. Utilizing the FIJI processing software, the thickness through which the β-tubulin III signal was present (indicating neural process extension) was measured and compared between PDMS and PDMS+CNT samples.

To measure the density of outgrowing β-tubulin III-positive neuronal fibers on PDMS and PDMS+CNT scaffolds, similar image stacks, as described above, with a z-step of 2 μm, were used. The FIJI software was used to measure the intensity of β-tubulin III-positive labeling of neuronal processes surrounding the spinal slice. The background intensity for each image was defined automatically by the software. The signal-positive area above the background threshold intensity was recorded to define the area of the image (depicted as a percentage of the total image area) positive for neuronal fibers (28 randomly sampled images from n=10 PDMS samples; 20 images from n=6 PDMS+CNT samples).

The alignment of fibers emerging from the spinal slices was quantified in terms of relative orientation by means of fiber directionality analysis [See ref.16 for detailed methods]. This was carried out using the Directionality plugin of Fiji software. Fourier component analysis is executed to identify orientation of ‘structures’; in our case β-tubulin III immunolabeled neuronal processes. Confocal images measuring 640 μm × 640 μm were used to compute mean fiber direction and the degree of dispersion (29 randomly sampled images from n=10 PDMS samples; 20 images from n=6 PDMS+CNT samples).

In vitro data statistical analysis

For all *in vitro* data, results are depicted as mean ± SE of the mean, unless otherwise stated; statistically significant differences between datasets were assessed

using Statistica software (StatSoft, Inc.). Student's t test (after validation of variance homogeneity by Levene's test) was used for parametric data, Mann-Whitney test for non-parametric data; results were further confirmed using MATLAB (http://www.mathworks.com). Differences in the relative cumulative frequency distribution were obtained using the paired Kolmogorov–Smirnov test. Chi-squared method analysis was performed for estimating significantly synchronous slices in the two groups (PDMS and PDMS+CNT) based on results obtained by the use of MATLAB. Statistical significance was established at $P<0.05$.

In vivo implantation of PDMS+CNT scaffold

All surgical procedures were performed on Wistar male rats (Harlan Laboratories; n=9, three animals per time point), 3 to 6 months of age and weighing 450 to 550 grams. Anesthesia was induced with Isofluorane (2% in 100% O_2, Sigma Aldrich) administered via a nose cone and maintained throughout the procedure. Anesthetic depth was monitored by checking the absence of tail and paw reflexes. The anesthetized animal was placed in a stereotaxic apparatus (Narishige SR-5R) and body temperature was maintained at 37 °C with a thermostatically controlled heating pad (temperature control unit HB 101/2; Panlab/Harvard Apparatus) to avoid anesthesia-induced hypothermia. Heart rate and oxygen saturation level were monitored via a pulse oxymeter (Pulsesense LS1P-10R, Nonin Medical Inc., Medair AB).

The implant consisted of a sharp-pointed cylinder (~2 mm in length and 0.5 ± 0.2 mm in diameter) carved out from a larger PDMS+CNT scaffold using a razor-blade and mounted on an electrode holder (ZIF-Clip, Tucker-Davis Technologies).[16]

Implant stiffness was increased via polyethylene glycol (PEG-8000, Sigma Aldrich) scaffold permeation after the carving procedure to facilitate subsequent insertion of the material into the brain tissue.

A square, 2 mm × 2 mm craniotomy was performed over the left hemisphere using a micro drill and the *dura mater* was removed, exposing the brain. Tissue adhesive (B. Braun Aeusculap, Germany) was applied on the inner perimeter of the craniotomy to prevent brain dimpling. The coordinates for implantation of the PEG-stiffened PDMS-CNT implant were A-P –4.5 mm from Bregma and M-L –3.5 mm and relate to the visual cortex (specifically the cortical junction between V2ML and V1)[50] in the adult rat. The scaffold was inserted via a micro-drive at a speed of about 0.5 mm/s to a depth of approximately D-V 2 mm until the material was completely within the cortical tissue. The high speed of insertion is necessary to prevent premature melting of the PEG. The craniotomy was filled with silicone (Kwik-Cast&Kwik-sil, World Precision Instrument) in order to isolate the exposed brain tissue and the skull surface covered by bone cement (Super Bond, C&B).

Throughout the procedure, the animal's eyes and cortex were periodically irrigated using an ophthalmic solution (Epigel, CevaVetem) and a 0.9% NaCl saline solution, respectively. Atropine (1.5 mg/kg) and Lactated Ringer's Solution (1 mL) were administered subcutaneously every hour to reduce secretions and maintain homeostasis. Analgesic solution (Rymadyl; 5 mg/kg, intraperitoneal) and antibiotic (Baytril; 5 mg/kg, intramuscular) were administered to the rat via injection immediately before the surgery and one hour prior to the end of the surgical procedure. Both solutions were administered following surgery via the animals' drinking water for three days post-surgery. Animals were monitored for recovery

immediately after the surgery and at least 3 times per day for the first 72 h. We used a general distress-scoring sheet (Institutional Standards for the Care and Use of Animals in Research and after consulting with a veterinarian) to assess pain and distress in animals using physiological (appearance) and behavioral (natural and provoked behavior) parameters. For each parameter a numerical score starting from 0 = normal, and reaching 3 = grossly abnormal, is determined. An extra point is added for each 3 given. The provoked behavior was tested after the first 72 h post implantation. This method allows an objective monitoring of animals general conditions, to evaluate the need of analgesics or euthanization. All the animals used in the study did not show any sign of pain or distress (score = 0). Following this 72 h period, animals were monitored once per day until sacrifice. Animals were sacrificed at 2, 4, and 8 weeks post-implantation.

Brain tissue preparation and immunohistochemistry

At the selected time points (2, 4, and 8 weeks post-implantation) animals were anesthetized with 5% chloral hydrate (7 mL/kg) and perfused transcardially with 0.1 M phosphate-buffered saline (PBS) followed by 4% paraformaldehyde in PBS. Brains were removed, post-fixed for 24 h at 4 °C in 4% PFA, and cryoprotected in 15% sucrose in PBS at 4 °C for 24 h and subsequently in 30% sucrose in PBS at 4 °C for at least 24 h. Brains were embedded in optimal cutting temperature (OCT) compound (Tissue-Tek), frozen at –20 °C, and sectioned at 25 µm horizontally onto SuperFrost-Plus slides (Thermo Scientific) using a cryostat.

Tissue-Tek was removed by PBS washing and tissue sections were protein-blocked in 3% bovine serum albumin (BSA), 3% fetal bovine serum (FBS), 0.3%

Triton X-100 in PBS for 30 min at room temperature. For primary antibody labelling, sections were incubated overnight at 4 °C with mouse anti-glial fibrillary acidic protein (GFAP; monoclonal, Sigma-Aldrich Cat# G3893, RRID: AB_477010; used at 1:200), rabbit anti-ionized calcium-binding adapter molecule 1 (Iba1; polyclonal, Wako Cat# 019-19741, RRID: AB_839504; used at 1:400), rabbit anti-β-tubulin III (1:250, Sigma), and/or mouse anti-neuronal nuclei (NeuN; polyclonal, Millipore Cat# MAB377, RRID: AB_2298772; used at 1:100) in 5% FBS in PBS. After washing in PBS, sections were incubated in secondary antibodies goat anti-rabbit AlexaFluor 594 (polyclonal, Thermo Fisher Scientific Cat# R37117, RRID: AB_2556545; used at 1:500) and goat anti-mouse AlexaFluor 488 (polyclonal, Thermo Fisher Scientific Cat# A-11029, RRID: AB_2534088; used at 1:500) in 5% FBS in PBS for 2 h at room temperature. Following final washing with PBS and water, tissue sections were covered with glass coverslips using Vectashield® hard mounting medium with DAPI (Vector Laboratories).

Brain tissue image acquisition and analysis

Immunoreactivity of the brain to the implanted material was measured by labeling tissue sections for reactive astrocytes and microglia using antibodies against GFAP and Iba1, respectively. Antibodies against β-tubulin III and NeuN were used to visualize neurons that may have infiltrated the scaffold. Fluorescence images were acquired using a Leica DM6000 upright microscope. In order to quantify GFAP and Iba1 labeling, a 10× dry objective was used to take images surrounding the entirety of the implanted material. Higher magnifications were used to take detailed images

for observation of cellular infiltration. Image analysis was performed using FIJI software.

For GFAP intensity measurements, 24 intensity profile lines were drawn at random intervals around the implanted material, starting from the edge of the implant and extending 500 μm into the surrounding tissue, as previously shown.[16] These lines produced a fluorescence intensity profile as a function of distance from the implant edge. To account for variations in labeling, an image of the contralateral hemisphere in the same anatomical region as the implanted material was taken at 10× and used to define the background intensity for each section (the fluorescence intensity was measured with 9 randomly placed intensity profile lines). In each tissue section, GFAP intensity values at each micron were calculated for 0 to 150 μm from the implant edge, normalized to the average intensity for the contralateral hemisphere, and finally averaged across all sections (n≥7) for each animal to create a mean intensity profile. Because differences in GFAP intensity were observed to be within 50 μm from the implant, for each animal the data from 0-150 μm were further normalized to the average intensity measured at 51 to 150 μm from the edge of the implant; these data were used for statistical analyses.[16]

For Iba1 intensity measurements, n=8 ROIs (100 μm × 500 μm) were selected starting from the edge of the implant and extending 500 μm into the surrounding tissue.[16] The background intensity threshold was defined for each section using the Iba1 labelling intensity measured in the contralateral hemisphere in the same anatomical region as the implanted material. The area within each ROI with intensity above the background threshold was calculated and used for statistics. The ROI for

all sections were averaged for each animal and are depicted as the mean ± standard error of the mean (SEM).

Statistical analysis was performed using Statistica software (StatSoft, Inc.). One-way analysis of variance (one-way ANOVA) was used to determine statistical significance at $P<0.05$, with post-hoc analysis performed using the Fisher's least significant difference (Fisher's LSD) method to compare datasets.

Ethics Statement

This study was carried out in accordance with the recommendations in the Guide for the Care and Use of Laboratory Animals of the National Institutes of Health and the appropriate international and institutional standards for the care and use of animals in research (Italian Ministry of Health, in agreement with the EU Recommendation 2007/526/CE). The protocols and all performed experiments are approved by the local veterinary service and the institutional (SISSA) ethical committee, in accordance with the EU guidelines (2010/63/UE) and Italian law (decree 26/14). All efforts were undertaken to minimize pain and suffering of the animals and to reduce the number of animals used.

Acknowledgements

E. R. A. and S. U. contributed equally to this work. The authors thank IOM-TASC (Trieste) for SEM assistance. We acknowledge the PRIN-MIUR n. 2012MYESZW, and the ByAxon n. 737116 to LB. MP, as the recipient of the AXA Chair, is grateful to the AXA Research Fund for financial support. MP was also supported by the Spanish Ministry of Economy and Competitiveness MINECO (project CTQ2016-76721-R), the University of Trieste and the Diputación Foral de Gipuzkoa program Red (101/16).

References

[1] U. Chaudhary, N. Birbaumer, A. Ramos-Murguialday, *Nat. Rev. Neurol.* **2016**, *12,* 513.

[2] J. P. Harris, D. J. Tyler, *Crit. Rev. Biomed. Eng.* **2013**, *41,* 435.

[3] C. H. Thompson, M. J. Zoratti, N. B. Langhals, E. K. Purcell, Tissue. Eng. Part B. Rev. **2016,** 22, 125.

[4] H. I. Chen, M. D. Jgamadze D Serruya, D. K. Cullen, J. A. Wolf, D. H. Smith, Front. Syst. Neurosci. **2016,** 10, 1.

[5] R. Green, M. R. Abidian, Adv. Mat. **2015**, 27, 7620.

[6] X. Duan, C. M. Lieber, Chem. Asian. J. **2013**, 8, 2304.

[7] S. Bosi, R. Rauti, J. Laishram, A. Turco, D. Lonardoni, T. Nieus, M. Prato, D. Scaini, L. Ballerini, *Sci. Rep.* **2015**, *24*, 9562.

[8] G. Cellot , E. Cilia, S. Cipollone, V. Rancic, A. Sucapane, S. Giordani, L. Gambazzi, H. Markram, M. Grandolfo, D. Scaini, F. Gelain, L. Casalis, M. Prato, M. Giugliano, L. Ballerini, *Nat. Nanotech.* **2009**, *4*, 126.

[9] G. Cellot, F. M. Toma, Z. K. Varley, J. Laishram, A. Villari, M. Quintana, S. Cipollone, M. Prato, L. Ballerini, *J. Neurosci.* **2011**, *31*, 12945.

[10] A. Fabbro, A. Villari, J. Laishram, D. Scaini, F. M. Toma, A. Turco, M. Prato, L. Ballerini, *ACS Nano* **2012**, *6*, 2041.

[11] A. Fabbro, A. Sucapane, F. M. Toma, E. Calura, L. Rizzetto, C. Carrieri, P. Roncaglia, V. Martinelli, D. Scaini, L. Masten, A. Turco, S. Gustincich, M. Prato, L. Ballerini, *PLoS One*, **2013**, *8*, e73621.

[12] V. Lovat, D. Pantarotto, L. Lagostena, B. Cacciari, M. Grandolfo, M. Righi, G. Spalluto, M. Prato, L. Ballerini, *Nano Lett.* **2005**, *5*, 1107.

[13] A. Mazzatenta, M. Giugliano, S. Campidelli, L. Gambazzi, L. Businaro, H. Markram, M. Prato, L. Ballerini, *J. Neurosci.* **2007**, *27*, 6931.

[14] D. Avossa, M. D. Rosato-Siri, F. Mazzaro, L. Ballerini, *Neuroscience* **2003**, *122*, 391.

[15] M. Heidemann, J. Streit, A. Tscherter, *Neuroscience* **2014**, *262*, 40.

[16] S. Usmani, E. R. Aurand, M. Medelin, A. Fabbro, D. Scaini, J. Laishram, F. B. Rosselli, A. Ansuini, D. Zoccolan, M. Scarselli, M. De Crescenzi, S. Bosi, M. Prato, L. Ballerini, *Science Adv.* **2016**, *2*, e1600087.

[17] B. H. Gähwiler, S. M. Thompson, D. Muller, *Curr. Protoc. Neurosci*. **2001**, *6*, 6.11.

[18] F. J. O'Brien, *Materials Today* **2011**, *14*, 88.

[19] E. Bracci, L. Ballerini, A. Nistri, *J Neurosci*. **1996**, *16*, 7063.

[20] L. Ballerini, M. Galante, *Eur. J. Neurosci*. **1998**, *10*, 2871.

[21] J. Streit, *J. Neurophysiol.* **1993**, *70*, 871.

[22] J. Zhou, D. A. Khodakov, A. V. Ellis, N. H. Voelcker, *Electrophoresis* **2012**, *33*, 89.

[23] K. J. Regehr, M. Domenech, J. T. Koepsel, K. C. Carver, S. J. Ellison-Zelski, W. L. Murphy, L. A. Schuler, E. T. Alarid, D. J. Beebe, *Lab Chip.* **2009**, *9*, 2132.

[24] R. N. Palchesko, L. Zhang, Y. Sun, A. W. Feinberg, *PLoS One* **2012**, *7*, e51499

[25] Minev IR, Musienko P, Hirsch A, Barraud Q, Wenger N, Moraud EM, Gandar J, Capogrosso M, Milekovic T, Asboth L, Torres RF, Vachicouras N, Liu Q, Pavlova N, Duis S, Larmagnac A, Vörös J, Micera S, Suo Z, Courtine G, Lacour SP, *Science* **2015,** *6218*, 159.

[26] Liu CX, Choi JW, *Conf Proc IEEE Eng Med Biol Soc.* **2009**, 6391.

[27] P. Fattahi, G. Yang, G. Kim, M. R. Abidian, *Adv. Mat.* **2014,** *26*, 1846.

[28] J. W. Han, K. Beomseok, L. Jing, M. Meyyappan, *Appl. Phys. Lett*. **2013**, *102*, 051903

[29] E. Berthier, E. W. Young, D. Beebe, *Lab Chip* **2012**, *12*, 1224.

[30] Pennisi CP, Zachar V, Gurevich L, Patriciu A, Struijk JJ, *Conf Proc IEEE Eng Med Biol Soc.* **2010**, 3804.

[31] Lu Y, Wang D, Li T, Zhao X, Cao Y, Yang H, Duan YY, *Biomaterials* **2009,** *25*, 4143.

[32] K. Zhou, S. Motamed, G. A. Thouas, C. C. Bernard, D. Li, H. C. Parkington, H. A. Coleman, D. I. Finkelstein, J. S. Forsythe, *PLoS One* **2016**, *11*, e0151589.

[33] E. R. Aurand, J. Wagner, C. Lanning, K. B. Bjugstad, *J. Funct. Biomat*. **2012**, *3*, 839.

[34] E. Fournier, C. Passirani, C. N. Montero-Menei, J. P. Benoit, *Biomaterials* **2003**, *24*, 3311

[35] G. C. McConnell, H. D. Rees, A. I. Levey, C. A. Gutekunst, R. E. Gross, R. V. Bellamkonda, *J. Neural. Eng.* **2009**, *6*, 056003.

[36] B. D. Winslow, M. B. Christensen, W. K. Yang, F. Solzbacher, P. A. Tresco, *Biomaterials* **2010**, *31*, 9163.

[37] S. M. Gutowski, K. L. Templeman, A. B. South, J. C. Gaulding, J. T. Shoemaker, M. C. LaPlaca, R. V. Bellamkonda, L. A. Lyon, A. J. García, *J. Biomed. Mater. Res. A* **2014**, *102*, 1486.

[38] V. S. Polikov, P. A. Tresco, W. M. Reichert, *J. Neurosci. Methods* **2005**, *148*, 1.

[39] A. A. Turner, M. Bouffard, H. C. Lukaski, Int. *J. Circumpolar Health* **1998**, *1*, 730.

[40] D. H. Szarowski, M. D. Andersen, S. Retterer, A. J. Spence, M. Isaacson, H. G. Craighead, J. N. Turner, W. Shain, *Brain Res.* **2003**, *983*, 23.

[41] J. K. Nguyen, D. J. Park, J. L. Skousen, A. E. Hess-Dunning, D. J. Tyler, S. J. Rowan, C. Weder, J. R. Capadona, *J. Neural. Eng.* **2014**, *11*, 056014.

[42] R. Biran, D. C. Martin, P. A. Tresco, *Exp. Neurol.* **2005**, *195*, 115.

[43] W. H. Chen, S. J. Cheng, J. T. Tzen, C. M. Cheng, Y. W. Lin, *PLoS One* **2013**, *8*, e83394.

[44] D. Paganin, S. C. Mayo, T. E. Gureyev, P. R. Miller, S. W. Wilkins, *J. Microsc.* **2002**, *206*, 33.

[45] F. Brun, S. Pacilè, A. Accardo, G. Kourousias, D. Dreossi, L. Mancini, G. Tromba, R. Pugliese, *Fundamenta Informaticae* **2015**, *141*, 233.

[46] F. Brun, L. Mancini, P. Kasae, S. Favretto, D. Dreossi, G. Tromba, *Nucl. Instr. Meth. Phys. Res. A* **2010**, *615*, 326.

[47] A. Odgaard, H. J. Gundersen, *Bone* **1993**, *14*, 173.

[48] W. B. Lindquist, S.-M. Lee, D. A. Coker, K. W. Jones, P. Spanne, *J. Geophys. Res.* **1996**, *101*, 8297.

[49] L. Ballerini, M. Galante, M. Grandolfo, A. Nistri, *J. Physiol.* **1999**, *517*, 459.

[50] G. Paxinos, C. Watson, *The Rat Brain in Stereotaxic Coordinates,* Elsevier Academic Press **2005**.

Figure 1. PDMS and PDMS+CNT scaffolds: SEM and µCT measures. (a) SEM micrograph of a PDMS scaffold slice showing the typical "sponge-like" aspect. The high-resolution image of the pore surface shown in the top-left inset highlights the PDMS smoothness. (b) SEM micrograph of a PDMS+CNT scaffold slice showing a similar porous morphology; a high-resolution image of the pore surface (top-left inset), nicely illustrates the carpet of MWCNTs decorating exclusively pores' walls and resulting in a rough surface. SEM images scale bar: 100 µm. Inset scale bars: 1 µm. (c) Left, an example of µCT volumetric reconstructions of scaffolds' pores and channelization in a ROI of 5123 voxels of the total volume. In blue and green, the maximal filling sphere for pore and throat diameter determinations, respectively, and in red, the interconnection path. Right, the scaffold's matrices (in white) are shown. Both samples show that all empty spaces inside the material are interconnected. (d) Histograms revealing that the two scaffolds have similar levels of porosity and isotropy. (e) Histogram showing the similar average values for pore diameters and throat diameters for both samples (n=3 for PDMS, n=3 for PDMS+CNT). Bars show mean ± SD values.

Figure 2. Three-dimensional distribution of neuronal processes extending from explanted spinal slices into PDMS or PDMS+CNT scaffolds. (a–b) β-Tubulin III-positive neuronal processes form vast networks when cultured on 3D PDMS (a) and 3D PDMS+CNT (b). Reconstruction of confocal image stacks permits visualization of the neurites as they penetrate the depth of the scaffolds (right panels in a and b). Scale bars: 50 µm. (c) Analysis of the depth through which β-Tubulin III-positive processes penetrate the scaffolds. (d) No differences were observed in β-Tubulin III

processes when evaluated as a percent of image area. (e) The degree of directionality dispersion, a measure of neuronal fiber orientation, indicated no differences between processes developed on PDMS or PDMS+CNT supports.

Figure 3. Electrophysiological activity of spinal slices on PDMS and PDMS+CNT scaffolds. (a) Organotypic spinal slices were cultured as pairs on the surface of a three-dimensional, micro-porous, PDMS scaffold (left) and of a PDMS+CNT (right) scaffold. Simultaneous extracellular recordings were taken from the ventral region of both slices. (b) Representative traces depict the disinhibited bursting activity of the slices. Arrowheads represent onset of each burst. Inter-event interval (IEI – time interval between two subsequent black arrowheads) is shown and measured as the time between the onset of one burst and the beginning of the next. (c) Relative cumulative frequency distributions of IEI values in slices grown in PDMS and in PDMS+CNT. For PDMS-CNT, the distribution of IEI values is significantly shifted to the left (K–S test; ***P<0.001).

Figure 4. PDMS+CNT scaffolds promote functional reconnection between organotypic spinal slice pairs *in vitro*. (a) Representative traces from simultaneous recordings of paired slices in PDMS (top) and PDMS+CNT (bottom), note the synchronous bursting in PDMS+CNT (left slice (L) right slice (R)). Red arrowheads indicate the onset of each burst in each slice. (b) Histograms represent the null distribution[12] of individual CCF values obtained from time windows independently sampled for the left and right recordings of both conditions; the red line indicates the average value of the actual CCF of sampled traces. Plots refer to the two explicative

traces shown in (a), and point to a significant synchronicity in PDMS+CNT traces (**P<0.01). (c) The fraction of correlated pairs was significantly greater in slice pairs cultured on PDMS+CNT; *P<0.05. (d) Distance between slices was not correlated to CCF, indicating that distance had no effect on synchronous activity. (e) Similar to distance, CCF did not correlate with the number of days *in vitro* of slice cultures.

Figure 5. Neuroimmune response to implanted PDMS+CNT scaffolds indicated that the scaffolds were largely biocompatible *in vivo*. (a) GFAP-positive astrocytes (green) were found in the cortex surrounding the PDMS+CNT implant at 2, 4, and 8 weeks post-implantation; (DAPI for nuclei is in blue). Boxed areas indicate magnified images shown in the insets. Scale bar: 200 µm and 50 µm (inset). (b) Iba1-positive microglia (red) were found surrounding the material as well as having infiltrated the scaffold; DAPI (blue). Boxed areas indicate magnified images shown in the insets. Scale bar = 200 µm and 50 µm (inset). (c) Increased GFAP immunoreactivity was observed primarily in the 50 µm immediately proximal to the implant. (d) Iba1-positive tissue immunoreactivity up to 500 µm from the edge of the implant was found to significantly decrease over time; *P<0.05, **P<0.01, ***P<0.001.

Figure 6. Neuronal infiltration of the PDMS+CNT scaffolds. (a) Left: low magnification of PDMS+CNT implant in the cortex after 2 weeks, the finding of β-tubulin III-positive cells (in red; the boxed area is magnified in the right panel) within the scaffold suggests that astrocytes and microglia cells surrounding the implant do not represent a barrier for neuronal infiltration; DAPI (blue). Scale bar: 200 µm (left) and 50 µm (right). (b) NeuN-positive neurons within the scaffold; DAPI (blue). Scale

bar: 50 µm. (c) β-tubulin III-positive cells invaded the implanted material as early as 2 weeks post-implantation and persisted at 4 and 8 weeks post-implantation.

Figure 1

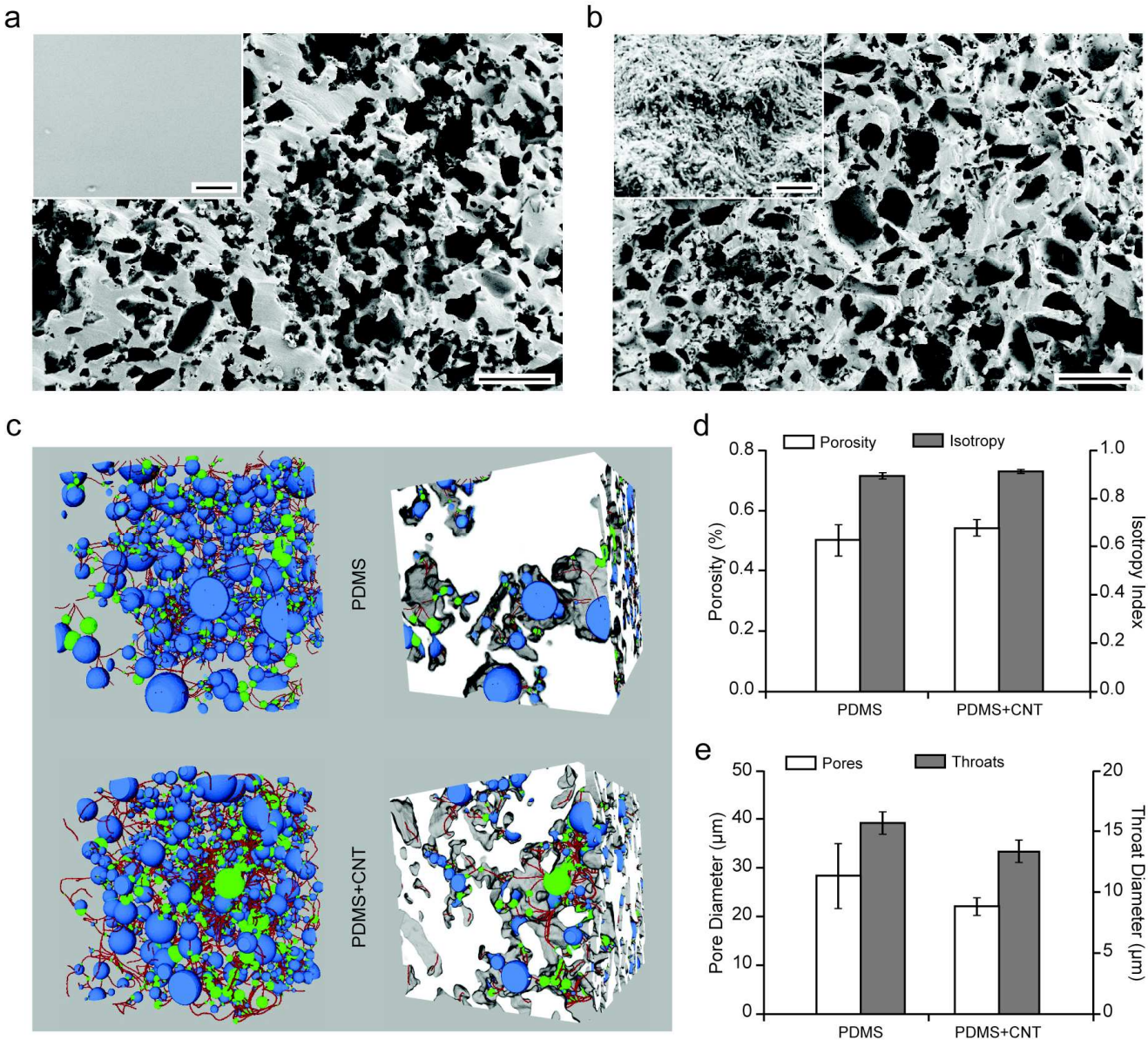
a
b
c
PDMS
PDMS+CNT
d
Porosity
Isotropy
Porosity (%)
Isotropy Index
0.0
0.2
0.4
0.6
0.8
1.0
PDMS
PDMS+CNT
e
Pores
Throats
Pore Diameter (µm)
Throat Diameter (µm)
0
10
20
30
40
50
0
5
10
15
20
PDMS
PDMS+CNT

Figure 2

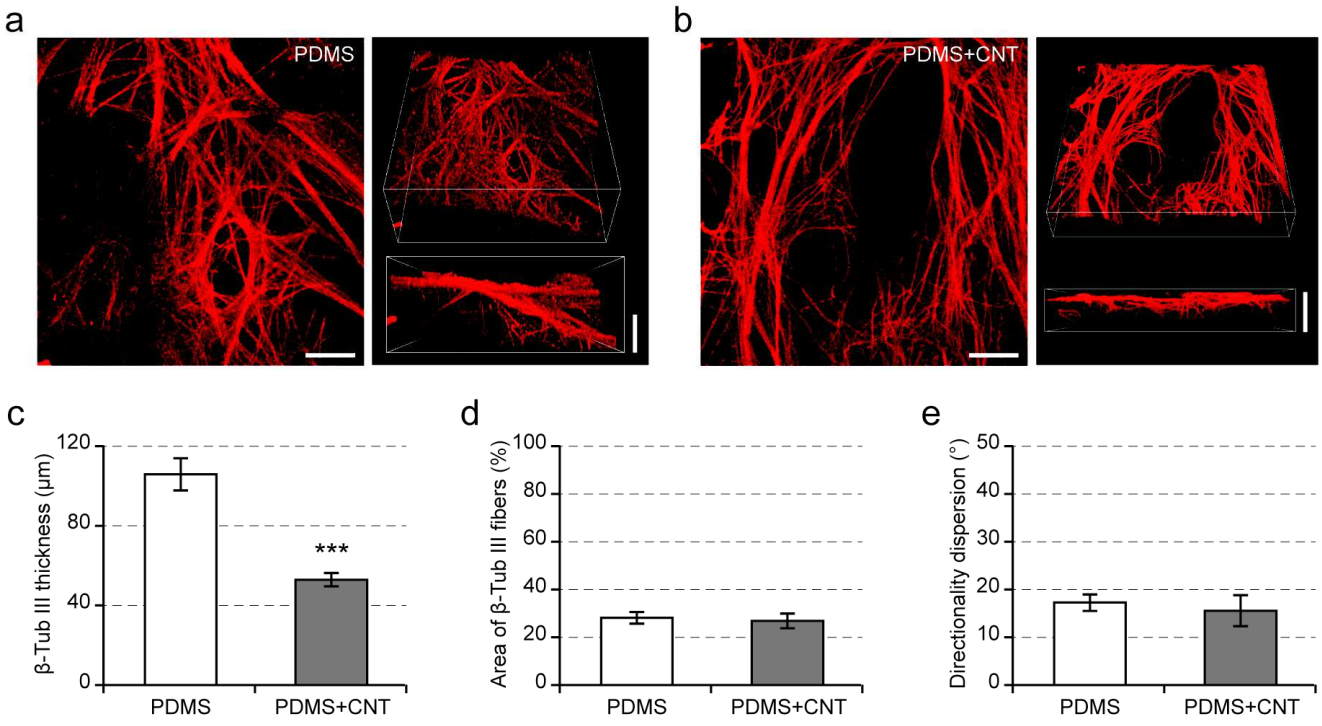
a
PDMS
b
PDMS+CNT
c
β-Tub III thickness (µm)
120
80
40
0
***
PDMS
PDMS+CNT
d
Area of β-Tub III fibers (%)
100
80
60
40
20
0
PDMS
PDMS+CNT
e
Directionality dispersion (°)
50
40
30
20
10
0
PDMS
PDMS+CNT

Figure 3

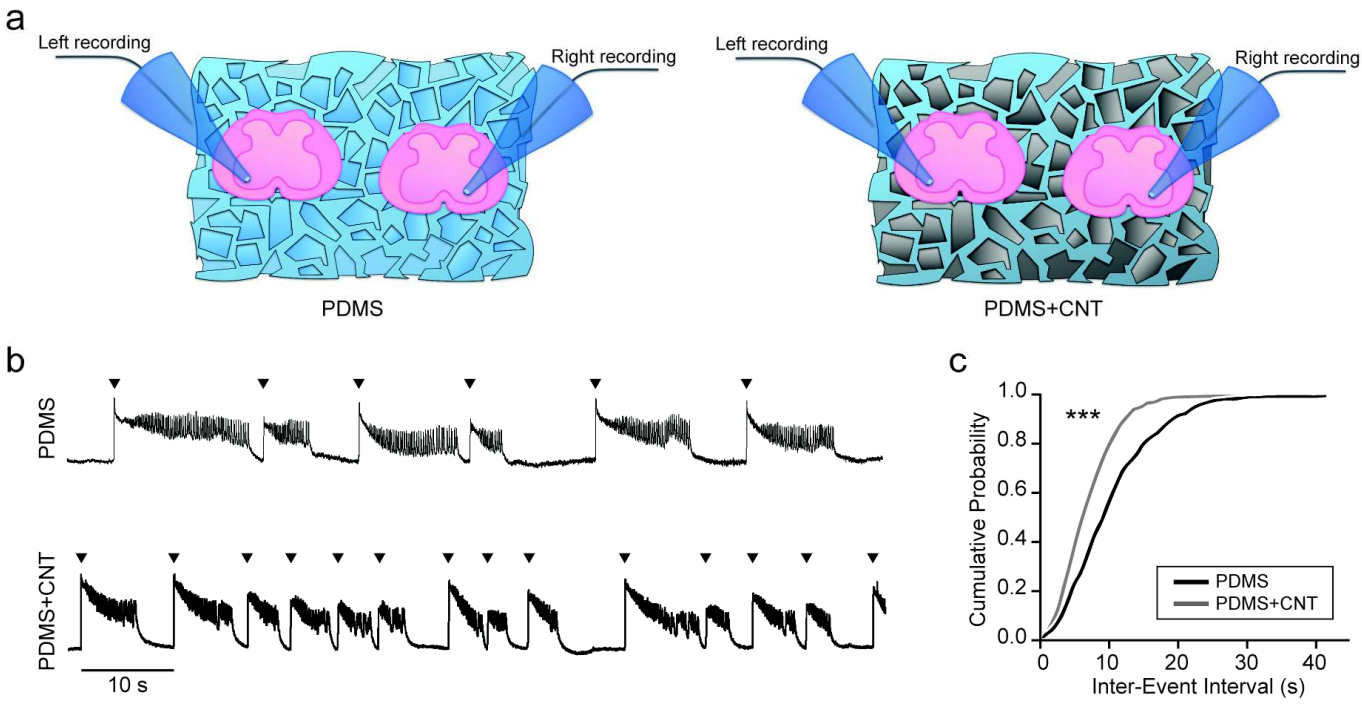
a
Left recording
Right recording
PDMS
Left recording
Right recording
PDMS+CNT
b
PDMS
PDMS+CNT
10 s
c
Cumulative Probability
1.0
0.8
0.6
0.4
0.2
0.0
***
PDMS
PDMS+CNT
0
10
20
30
40
Inter-Event Interval (s)

Figure 4

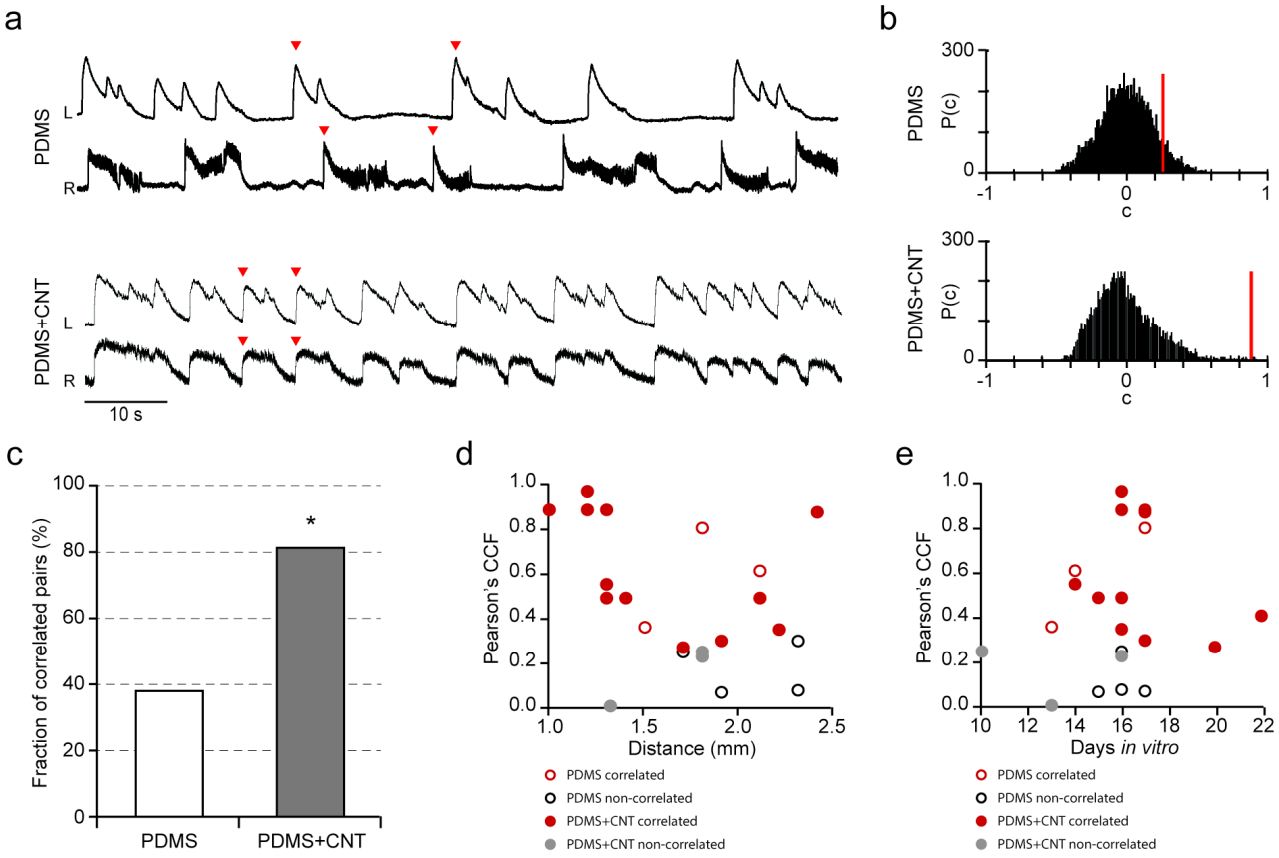
a
PDMS
L
R
PDMS+CNT
L
R
10 s
b
PDMS
P(c)
300
0
-1
0
1
c
PDMS+CNT
P(c)
300
0
-1
0
1
c
c
Fraction of correlated pairs (%)
100
80
60
40
20
0
*
PDMS
PDMS+CNT
d
Pearson's CCF
1.0
0.8
0.6
0.4
0.2
0.0
1.0
1.5
2.0
2.5
Distance (mm)
PDMS correlated
PDMS non-correlated
PDMS+CNT correlated
PDMS+CNT non-correlated
e
Pearson's CCF
1.0
0.8
0.6
0.4
0.2
0.0
10
12
14
16
18
20
22
Days in vitro
PDMS correlated
PDMS non-correlated
PDMS+CNT correlated
PDMS+CNT non-correlated

Figure 5

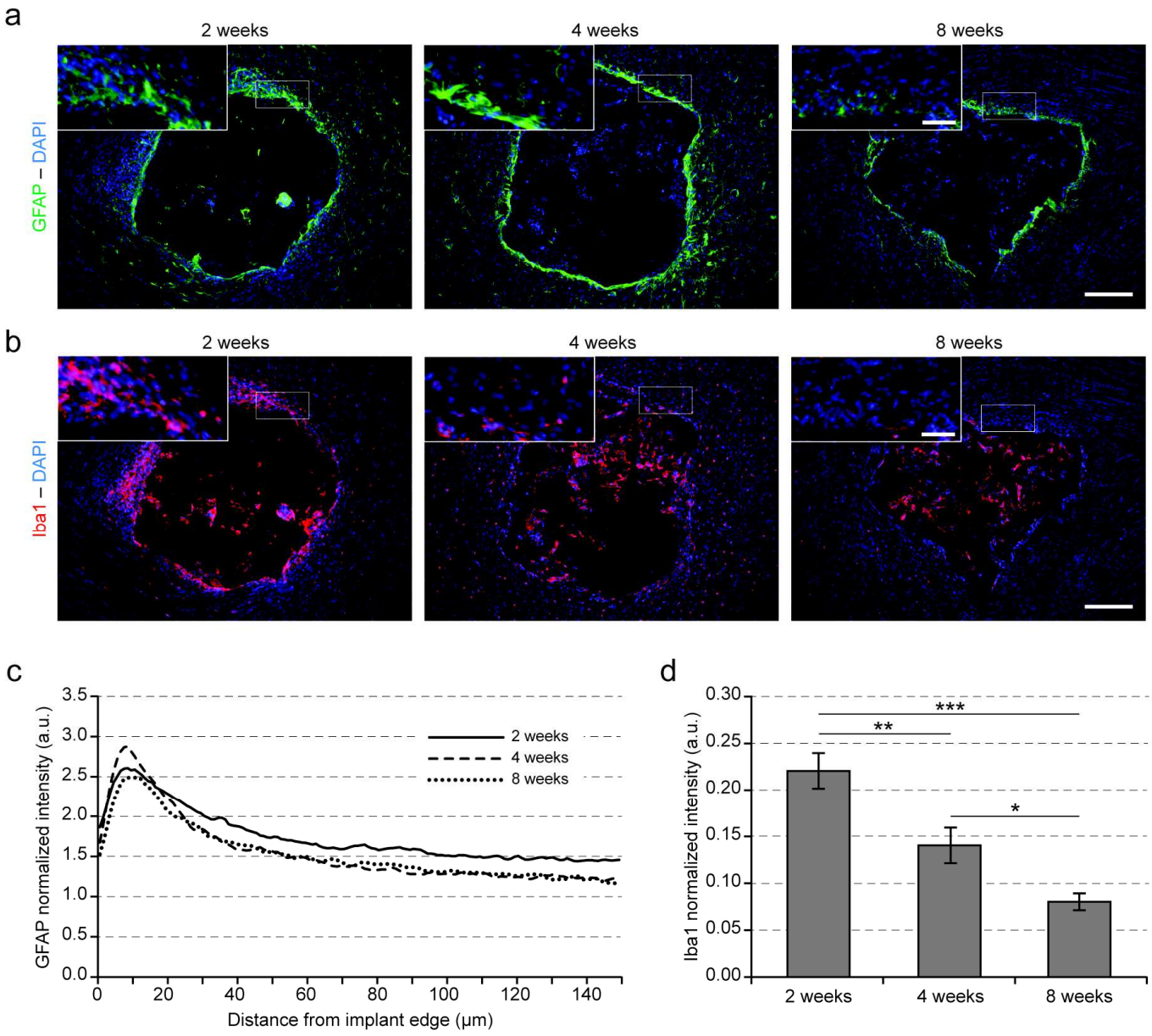
a
2 weeks
4 weeks
8 weeks
GFAP – DAPI
b
2 weeks
4 weeks
8 weeks
Iba1 – DAPI
c
GFAP normalized intensity (a.u.)
3.5
3.0
2.5
2.0
1.5
1.0
0.5
0.0
0
20
40
60
80
100
120
140
Distance from implant edge (µm)
2 weeks
4 weeks
8 weeks
d
Iba1 normalized intensity (a.u.)
0.30
0.25
0.20
0.15
0.10
0.05
0.00
***
**
*
2 weeks
4 weeks
8 weeks

Figure 6

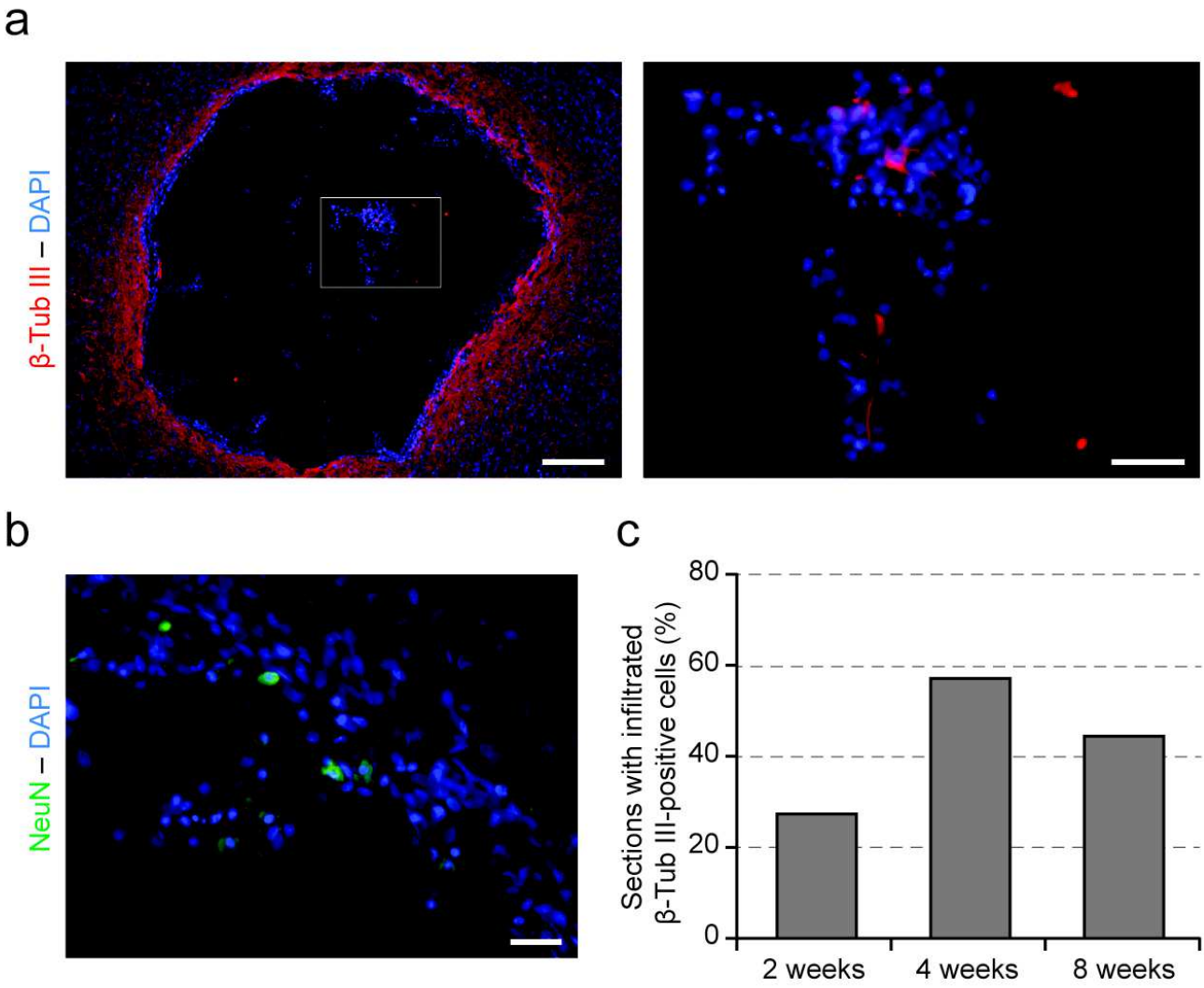
a
β-Tub III – DAPI
b
NeuN – DAPI
c
Sections with infiltrated β-Tub III-positive cells (%)
80
60
40
20
0
2 weeks
4 weeks
8 weeks